ARTICLE IN PRESS

Phytochemistry xxx (2009) xxx–xxx

Contents lists available at ScienceDirect

Phytochemistry

journal homepage: www.elsevier.com/locate/phytochem

The hyperaccumulator *Alyssum murale* uses complexation with nitrogen and oxygen donor ligands for Ni transport and storage

David H. McNear Jr. [a,*], Rufus L. Chaney [b], Donald L. Sparks [c]

[a] *Rhizosphere Science Laboratory, Department of Plant and Soil Sciences, University of Kentucky, N122S Agricultural Sciences North Building, 1100 Nicholasville Road, Lexington, KY 40546-0091, USA*
[b] *USDA-ARS, Environmental Management and Byproducts Laboratory, Beltsville, MD 20705, USA*
[c] *Environmental Soil Chemistry Research Group, Department of Plant and Soil Sciences, University of Delaware, 152 Townsend Hall, Newark, DE 19717-1303, USA*

ARTICLE INFO

Article history:
Received 26 February 2009
Received in revised form 23 September 2009
Accepted 26 October 2009
Available online xxxx

Keywords:
Alyssum murale
Hyperaccumulation
Nickel (Ni)
Extended X-ray absorption fine structure (EXAFS) spectroscopy
Synchrotron X-ray fluorescence (SXRF) spectroscopy
Tolerance
Malate
Histidine

ABSTRACT

The Kotodesh genotype of the nickel (Ni) hyperaccumulator *Alyssum murale* was examined to determine the compartmentalization and internal speciation of Ni, and other elements, in an effort to ascertain the mechanism used by this plant to tolerate extremely high shoot (stem and leaf) Ni concentrations. Plants were grown either hydroponically or in Ni enriched soils from an area surrounding an historic Ni refinery in Port Colborne, Ontario, Canada. Electron probe micro-analysis (EPMA) and synchrotron based micro X-ray fluorescence (μ-SXRF) spectroscopy were used to determine the metal distribution and co-localization and synchrotron X-ray and attenuated total reflectance-Fourier transform infrared (ATR-FTIR) spectroscopies were used to determine the Ni speciation in plant parts and extracted sap. Nickel is concentrated in the dermal leaf and stem tissues of *A. murale* bound primarily to malate along with other low molecular weight organic ligands and possibly counter anions (e.g., sulfate). Ni is present in the plant sap and vasculature bound to histidine, malate and other low molecular weight compounds. The data presented herein supports a model in which Ni is transported from the roots to the shoots complexed with histidine and stored within the plant leaf dermal tissues complexed with malate, and other low molecular weight organic acids or counter-ions.

© 2009 Elsevier Ltd. All rights reserved.

1. Introduction

There is much to be learned about the biochemical or physiological mechanisms responsible for excess metal uptake and storage in hyperaccumulating plants. Understanding these mechanisms would be beneficial for increasing the efficiency of current hyperaccumulating cultivars or transferring this quality to higher biomass, faster growing and climactically adapted plant species for use in either phytoremediation or phytomining of metal-enriched soils across a variety of landscapes. Improving our understanding of metal physiology in hyperaccumulating plants will also assist in efforts to fortify staple agronomic food crops with essential metal micro-nutrients (e.g., Zn, Fe) (White and Broadley, 2009).

A component of deciphering the biochemical and/or physiological mechanisms responsible for metal hyperaccumulation is determining where and in what chemical form the metal is being stored and how it is translocated from the root zone to these locations. There have been a number of studies directed at elucidating these mechanisms which established that a plant's ability to hyperaccumulate metals can depend on the plant species, the chemical properties of the element being detoxified (Assuncao et al., 2003) or, in some cases, tissue type and age (Kupper et al., 2004). For Ni (and other transition metals), most studies have implicated oxygen or nitrogen donor ligands such as citrate, malate, malonate or histidine as the compounds responsible for transport and storage of the metal. Histidine, in the Ni hyperaccumulator *Alyssum lesbiacum*, is the only amino acid shown to increase in xylem sap in response to increased metal concentrations in the growth media (Kramer et al., 1996). There is no evidence to support that endogenous overproduction of either organic or amino acids are a specific response resulting from elevated metal exposure. Instead, selected hyperaccumulators have been found to have a constant and unusually high organic and/or amino acid concentration which implies that excess metal accumulation in some species may be a constitutive property (Boyd and Martens, 1998; Ostergren et al., 1999). In this case, tolerance to internally high heavy metal concentrations, perhaps as an evolutionary adaptation to growing either on metal rich soils or in response to selective pressures from herbivores, would be a sufficient explanation for increased metal uptake.

* Corresponding author. Tel.: +1 859 257 8627.
E-mail address: dave.mcnear@uky.edu (D.H. McNear).

0031-9422/$ - see front matter © 2009 Elsevier Ltd. All rights reserved.
doi:10.1016/j.phytochem.2009.10.023

Please cite this article in press as: McNear, D.H., et al. The hyperaccumulator *Alyssum murale* uses complexation with nitrogen and oxygen donor ligands for Ni transport and storage. Phytochemistry (2009), doi:10.1016/j.phytochem.2009.10.023

In some plants, the cysteine-containing metal binding ligands metallothioneins (MT) and phytochelatins (PC) have been shown to play a role in metal tolerance when accumulated metals are at phytotoxic levels, but less so in metal tolerant plants (Schat et al., 2002). Phytochelatins are comprised of cysteine, glycine and glutamate and are used in algae and plants to detoxify excess cellular metal. PCs are readily produced in metal stressed, non-hypertolerant organisms (plants, insects), but their production in hypertolerant species is only inducible at extremely high exogenous metal concentration (Schat et al., 2002; Ebbs et al., 2002). Therefore, it is unlikely that they have a direct role in transition metal tolerance in hyperaccumulating plants. Phytochelatins have been found to have a role in the detoxification of arsenic in *Pteris vittata* (Chinese Brake fern), which several researchers have shown to have inducible PC production (Zhang and Cai, 2003).

Nickel hyperaccumulating plants have been the most studied of the hyperaccumulators, likely because over three quarters of the roughly 450 metal hyperaccumulators identified to date are hyperaccumulators of Ni. In the current paper, we investigated the biochemical mechanisms of Ni hyperaccumulation in *Alyssum murale*; one of the few hyperaccumulators to be developed as a commercial crop for the removal of metals from metal-enriched soils (Zhang et al., 2007). *A. murale* is native to Mediterranean serpentine soils and has the ability to hyperaccumulate Ni and Co (Broadhurst et al., 2004b), using different mechanisms to tolerate each.

Tappero et al. (2007), using a variety of techniques, examined the co-tolerance mechanisms in *A. murale* exposed to different combinations of Zn, Co and Ni. They showed that *A. murale* does not hyperaccumulate Zn and stores Co in the apoplasm of leaf mesophyll, in the leaf tips and possibly as extracellular precipitates on the leaf surface. They found that exposure of *A. murale* to either Zn or Co had no effect on the amount and localization of Ni within the plants, that Zn was not accumulated, nor did it interfere with Ni uptake, finally concluding that *A. murale* used different tolerance mechanisms for Co and Ni. Broadhurst et al. (2004b, 2009), using scanning electron microscopy with energy dispersive X-ray detection (SEM/EDX), also reported that *A. murale* preferentially stores Mn in the basal compartments of the Ca rich leaf trichomes. From these studies, it is apparent that different biochemical mechanisms govern the way in which *A. murale* tolerates each of these metals.

More is known about the chemical mechanisms used for Ni tolerance in *A. murale* compared to either Mn or Co. Nickel accumulates primarily in the cell vacuoles of epidermal stem and leaf tissues and trichome basal compartments (Broadhurst et al., 2004a; McNear et al., 2005), with palisade mesophyll cells becoming important only at higher soil Ni concentrations probably resulting from overflow of the primary cellular storage compartments (Broadhurst et al., 2004a). The transport and storage of Ni in several *Alyssum* species has been attributed to organic acids and possibly histidine. Little information has been reported, however, on the mechanism used by *A. murale* to tolerate such high Ni concentrations, let alone the chemical mechanism used to tolerate Co, Mn and Ca. Montargès-Pelletier et al. (2008) using unfocused (*bulk*) synchrotron X-ray spectroscopy found that *A. murale* stored Ni in its leaves as Ni–malate and in the stems as Ni–citrate complexes. The bulk X-ray methods used in their studies relied on dried and homogenized tissues which provided a good measure of the average Ni speciation present in the plant tissues. One drawback, as pointed out by Sarret et al. (2002), when analyzing ground and homogenized plant samples, is the possibility that contents of different cellular compartments can come into contact and thus change the metal speciation. In addition, in heterogeneous materials like plant tissues, where the metal speciation can vary over microns depending on the tissue it is found in, bulk-EXAFS spectroscopy may not adequately ascertain the minor metal complexes which may have a major role in the plants mechanisms of detoxification, transport or storage. The authors themselves note this limitation and state that microbeam methods are necessary to "unravel the complete Ni pathway".

The objectives of this research were to perform a detailed characterization of the chemical mechanisms responsible for the transport and storage of Ni in the 'Kotodesh' genotype of the Ni hyperaccumulator *A. murale* using a combination of synchrotron based microspectroscopic techniques, electron microscopy and Fourier transform infrared spectroscopy, respectively.

2. Results

2.1. Element distribution and compartmentalization

Fig. 1a is a false colored confocal micrograph showing the primary fluorescence generated from the different tissue types within a leaf from *A. murale* and is provided here to highlight the location of the epidermal and vascular tissues (green[1]) in relation to the mesophyll (red). Presented in Fig. 1b is the scanning electron micrograph (SEM) of an entire leaf cross-section with boxes highlighting examples of the regions analyzed in Fig. 1c and d. Fig. 1c and d presents the backscattered electron (BSE; large) and energy dispersive (EDS; small) micrographs of mid-leaf and mid-rib cross-sections. Ni is located in the dermal tissues, vascular bundles, mid-rib and leaf veins (Fig. 1c and d), and is absent from the mesophyll. Sulfur and potassium are concentrated in the mesophyll and calcium to the leaf surface, none of which are correlated with Ni. The distribution of Mn is less obvious from Fig. 1c, although Mn does appear more enriched in the dermal tissues than the mesophyll. Fig. 2a–f presents the synchrotron based X-ray fluorescence spectroscopy (SXRF) images simultaneously showing the distribution of Ni, Mn and Ca within several leaves from soil and hydroponically grown *A. murale* plants. Ni appears evenly distributed throughout all of the leaves, with enrichment in the vascular tissues (Fig. 2a, b and f), as well as an apparent enrichment in the leaf margins (Fig. 2b, e and c). Vascular enrichment was observed with SEM in this study and others (McNear et al., 2005; Tappero et al., 2007) and is not interpreted as Ni bound to vascular tissues. Instead, because the leaves were analyzed relatively fresh (i.e., removed from the plant just prior to analysis), Ni was likely trapped there upon freezing. The apparent enrichment of the leaf margins is likely an aberration of the 2D technique resulting because the X-ray beam samples a larger volume of dermal tissue (which was noted to contain the most Ni) at these locations compared to others. For example, the influence of sample volume on fluorescence response is apparent in Fig. 2a, where the leaf tip was folded over and the X-ray beam sampled two layers of leaf tissue resulting in higher relative fluorescence from this region. Similar to the study of Broadhurst et al. (2004), Mn (green) was found to be localized in the region of the Ca rich trichomes (blue) on the leaf surface of *A. murale*.

2.2. Spectroscopic characterization of standards

The ATR-FTIR spectra for oxalate, malonate, acconitate, citrate, malate, tartrate, histidine and each with and without Ni, are shown in Fig. 3. For all IR spectra (Fig. 3), the region between 1000 and 1800 cm^{-1} (i.e., near-IR region) was isolated because it provided the most information about the coordination environment of the metal complexes with the functional groups found in organic and amino acids. The pH of the aqueous standards was adjusted to match the pH found in typical plant xylem (i.e., pH

[1] For interpretation of color in Figs. 1 and 2, the reader is referred to the web version of this article.

Please cite this article in press as: McNear, D.H., et al. The hyperaccumulator *Alyssum murale* uses complexation with nitrogen and oxygen donor ligands for Ni transport and storage. Phytochemistry (2009), doi:10.1016/j.phytochem.2009.10.023

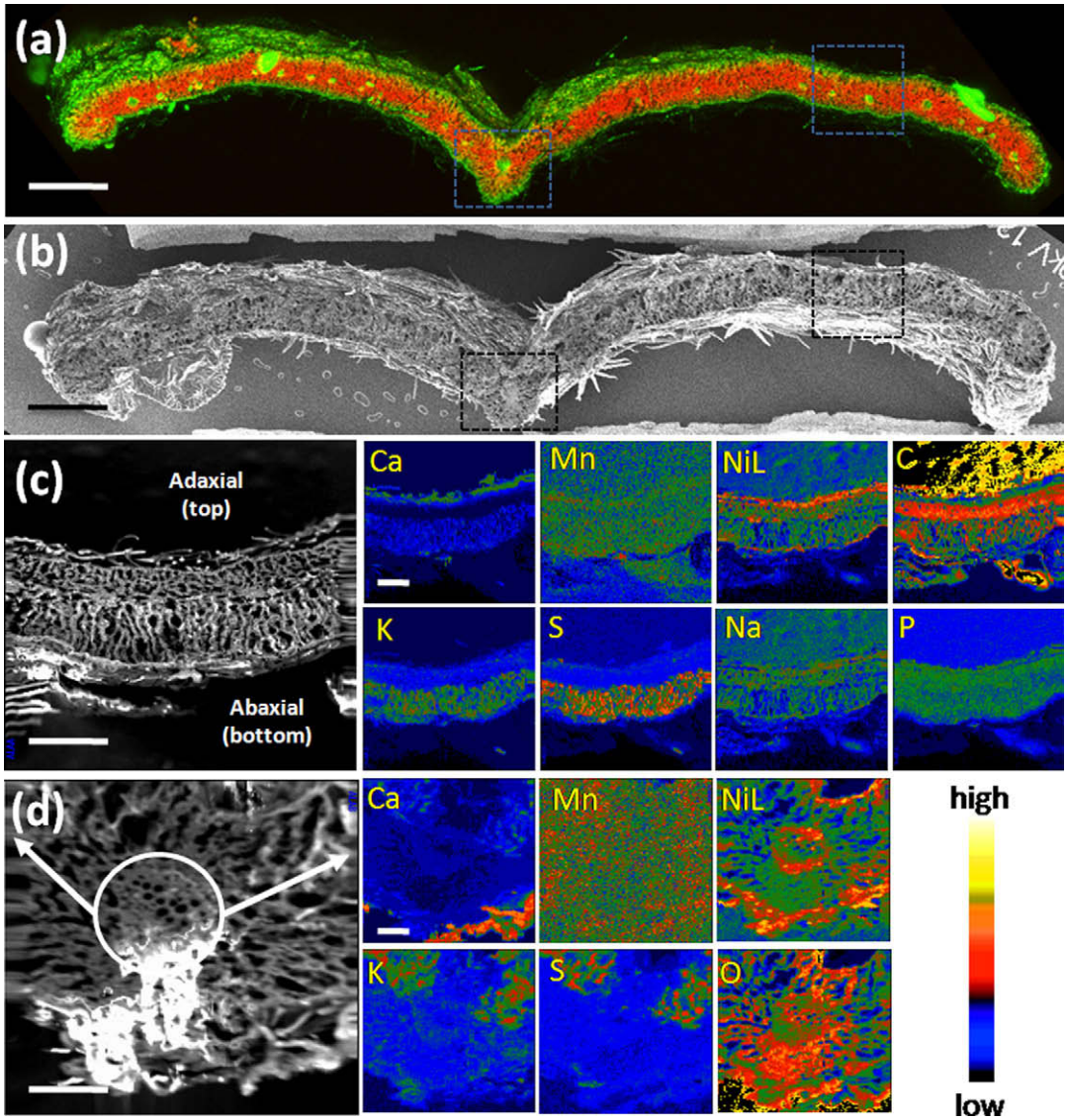

Fig. 1. Panels (a) and (b) show a laser scanning confocal micrograph and backscatter electron (BSE) image of an *Alyssum murale* leaf cross-section, respectively (bar = 250 μm). Panels (c) and (d) show a BSE close-up (large) and energy dispersive spectroscopy (EDS) elemental distribution maps (small) through the mid-leaf (c) and mid-rib regions (d) (bar = 20 μm), of an *A. murale* leaf cross-section (boxes in panels (a) and (b) indicate regions analyzed in panels (c) and (d)). The circle in panel (c) indicates the location of the vascular tissue and the arrows point in the direction of the leaf margin.

6.5–7.0). At these values, all of the carboxyl groups of the organic and amino acids are expected to be fully deprotonated in Ni free solutions. For the Ni-organic/amino acid complexes, the ligand was provided in considerable excess (4–10×) in order to assure that the standard represented the fully complexed Ni-organic/amino acid species.

In general, the IR features (Fig. 3) occurring between 1690–1750 and 1200–1300 cm^{-1} are attributed to carbonyl stretching (νC=O) and C–OH vibrations (νC–OH) of the protonated carboxylate anion (Cabaniss et al., 1998). Upon deprotonation, the νC=O stretching mode becomes more symmetric and shifts to higher energy and the asymmetric mode of the νC–OH to lower energy. Shifts in this region are most notable for oxalate followed by citrate and malate indicating the involvement of one or more carboxyl groups in the complexation of Ni by these stronger metal chelates. Conversely, the aconitate spectra changes very little with Ni addition indicating only a week, outer sphere association between the two. Changes in the 1300–1500 cm^{-1} range of the malonate spectra, notably the peak at 1440 cm^{-1}, are attributed to dipole moment changes resulting from straining of the central $-CH_2$ group most likely from Ni complexation with the two malonate carboxyl groups forming a mononuclear, bidentate configuration (Dobson and McQuillan, 1999). For the organic acids malate, tartrate, citrate and the amino acid histidine (Fig. 3), absorption bands between 1000 and 1200 cm^{-1} were observed which may be attributed to the C–O stretching of the intermediary alcohol groups (ν_α(C–OH)) (Cabaniss and McVey, 1995) or, for histidine, C–N stretching (ν(C–N)). Also in the histidine IR spectra (Fig. 3) were absorption bands at 1602 and 1518 cm^{-1} associated with the imidazole ring motion and ring vibration, respectively.

The IR spectrum for cysteine (Fig. 3) contains absorption bands at ~1600 and 1400 cm^{-1} representing the ν_{as}(C–OH) and ν_s(C–OH) stretching modes, respectively, of the carboxyl group. The bands remain virtually unchanged after Ni addition indicating that the carboxyl group is not participating in Ni complexation. The absorption band at 1620 cm^{-1} result from interactions with the amine group (δ(NH)) and is shifted to lower energy after complexation with Ni. The sharp peaks below the ν_{as}(C–OH) band at

Please cite this article in press as: McNear, D.H., et al. The hyperaccumulator *Alyssum murale* uses complexation with nitrogen and oxygen donor ligands for Ni transport and storage. Phytochemistry (2009), doi:10.1016/j.phytochem.2009.10.023

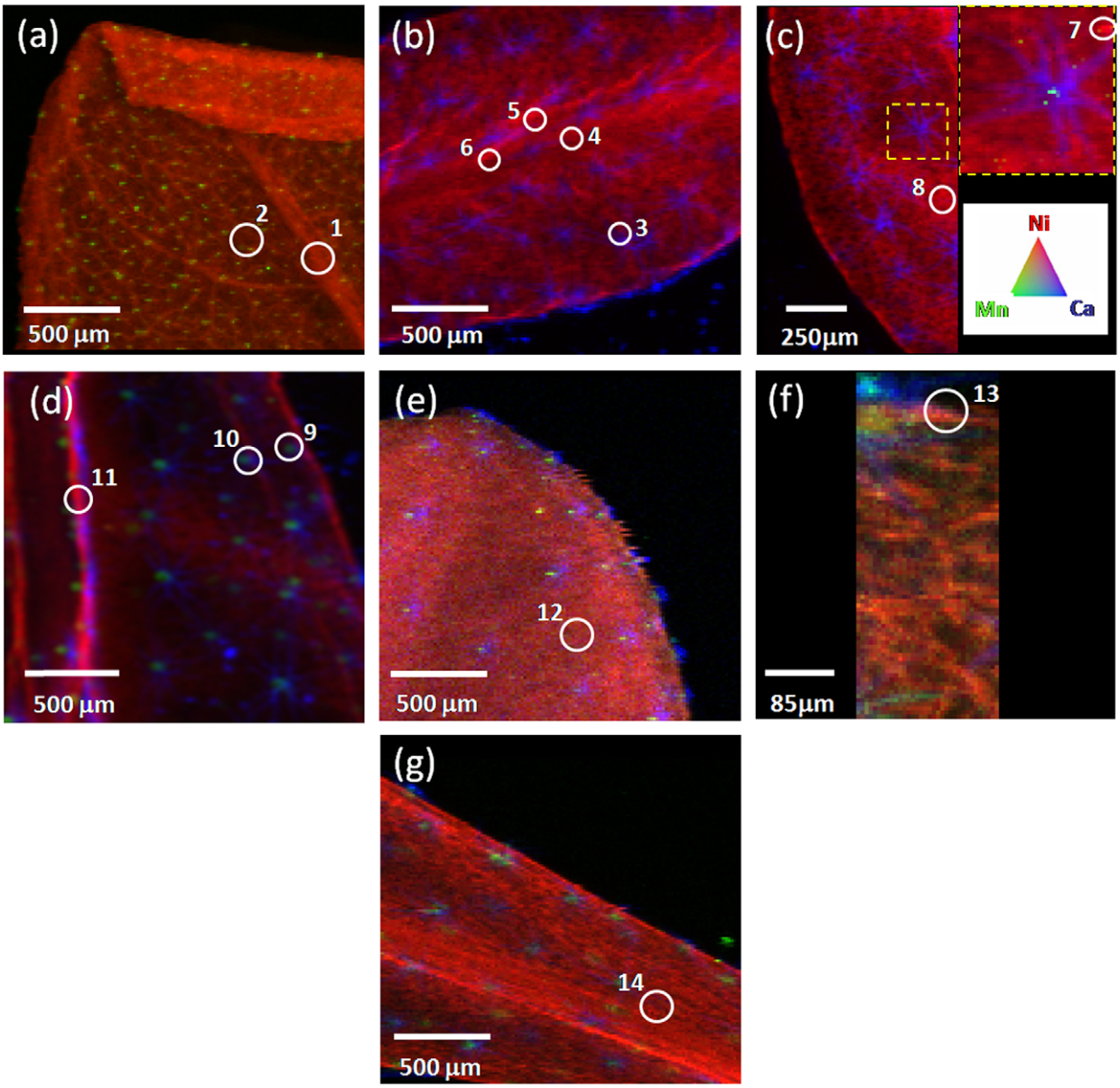

Fig. 2. (a–g) Micro-SXRF tricolor maps of leaves from *Alyssum murale*. Red, green and blue indicate the distribution of Ni, Mn and Ca, respectively. The numbered circles indicate locations where micro-EXAFS spectra were collected which are shown in Fig. 5. The yellow box in panel (c) indicates the location where a finer map was collected which is shown in the upper right of the panel.

1400 cm^{-1}, specifically bands at 1348 and 1302 cm^{-1}, whose intensity increases upon complexation with Ni are likely due to either bending or twisting modes of the coordinating amine group (Pawlukojc et al., 2005; Ramos et al., 2008). From the IR data, it is difficult to assess the involvement of S in the complexation of Ni as the associated IR bands appear around 300 cm^{-1} and which is below the resolution of the instrument. No IR spectra were collected for either Ni–glutathione or Ni–glycine.

Fig. 4 shows the XANES, $k^3\chi(k)$-spectra and radial structure functions (RSF) for the organic reference phases, and *Table* S1 (Supplementary data), the results from non-linear least squares fitting. Notable features in these spectra, which indicate the formation of stronger metal ligand complexes, include a widening of the first primary absorption peak at 8.33 keV and a shoulder between 8.34 and 8.35 keV in the XANES spectra (arrows Fig. 4a) and the appearance of a pronounced second shell carbon contribution in the RSF (Fig. 4c). Strathmann and Myneni (2004), using both FTIR and synchrotron X-ray spectroscopy to characterize the binding environment of Ni with several organic acids, noted that longer chain organic acids, where the carboxylate functional groups are separated by one or more methylene groups form weak complexes with Ni and thus have spectra similar to that of the hydrated Ni species. However, those organic or amino acids with shorter chains or closely packed carboxyl (COOH) groups supported by adjacent alcohol (α(C–OH)) donor groups or ring structures (e.g., the imidazole ring of histidine) form more rigid bonds (i.e., stronger complexes) leading to the diagnostic spectral features described previously. Supporting these observations (*Table* S1 Supplementary data), only the first coordination shell of oxygen could be fit ($CN_{Ni-O} \approx 6$; $R_{Ni-O} = 2.05$ Å) for Ni–succinate, Ni–aconitate and the aqueous Ni standard while the remaining organic/amino acid standards (histidine, malate, malonate, citrate, oxalate, tartrate, cysteine and glycine) all had significant second shell carbon contributions ($CN_{Ni-C} \approx 1.9$–5.5; $R_{Ni-C} \approx 2.82$–2.92) (see Supplemental data for further fitting details).

Please cite this article in press as: McNear, D.H., et al. The hyperaccumulator *Alyssum murale* uses complexation with nitrogen and oxygen donor ligands for Ni transport and storage. Phytochemistry (2009), doi:10.1016/j.phytochem.2009.10.023

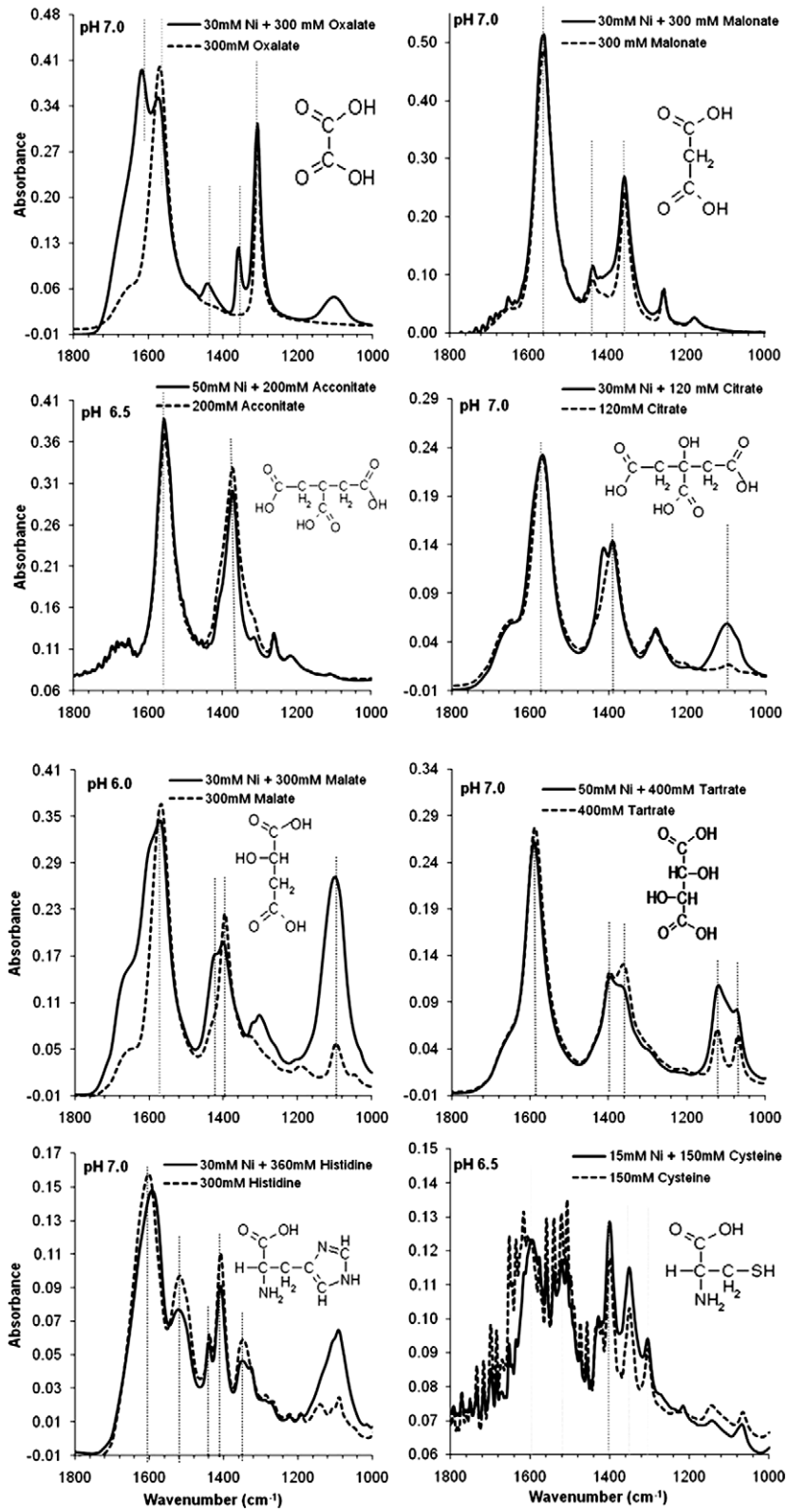

Fig. 3. ATR-FTIR near-IR spectra for selected organic/amino acids with and without Ni. Dotted lines indicate regions where significant changes have occurred.

Additional diagnostic features in the include asymmetry in the oscillations between 3 and 7 Å^{-1} in the $k^3\chi(k)$-spectra (arrows Fig. 4b). Montargès-Pelletier et al. (2008), using multiple Fourier back-filtering ranges of the RSF, demonstrated for the Ni–citrate standard that the asymmetry that occurs in the 3–7 Å^{-1} region of the $k^3\chi(k)$-spectra can be attributed to C or O atoms beyond the second coordination shell. Extending the Fourier filtering range beyond 4 Å, while certainly contributing to the features in the overall $k^3\chi(k)$-spectra, had more of an influence at higher k ranges (i.e., >10) in the $k^3\chi(k)$-spectra. Therefore, the features between 3 and

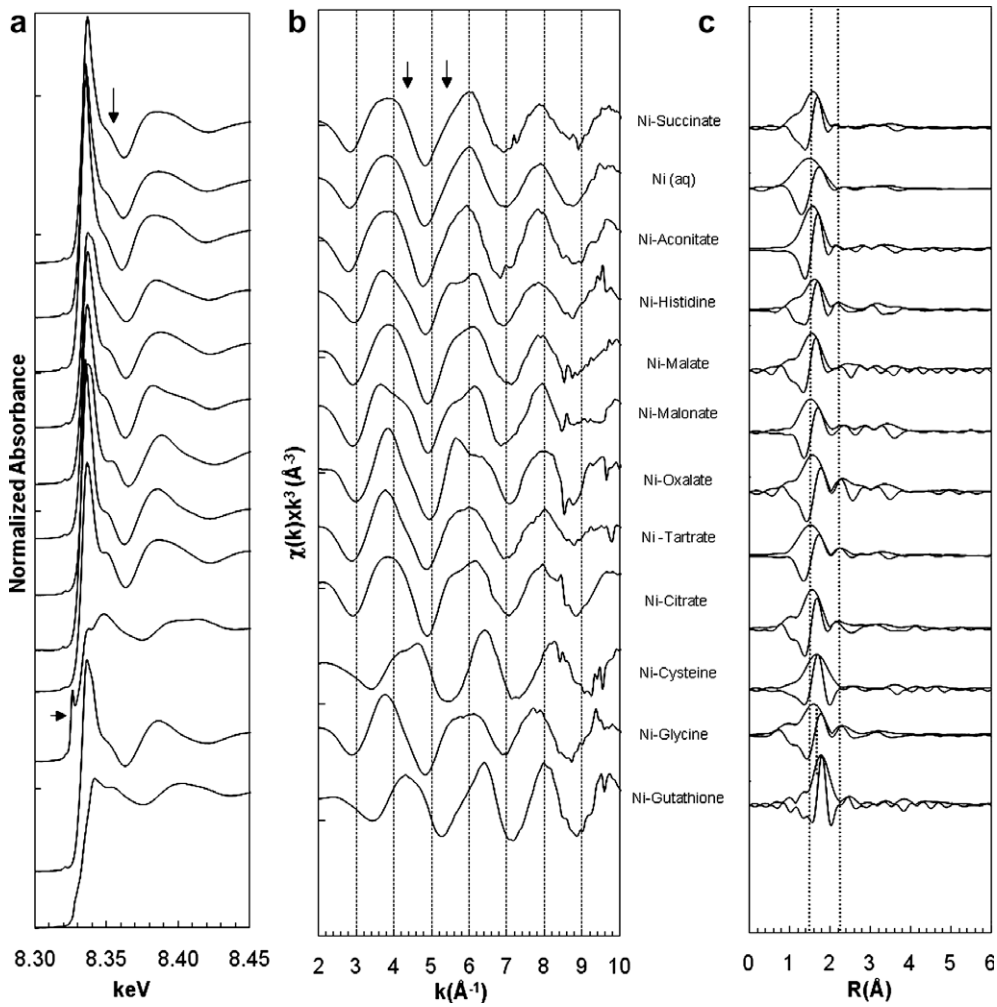

Fig. 4. (a) X-ray absorption near-edge spectra (XANES), (b) $k^3\chi(k)$-spectra and (c) radial structure functions of Ni aqueous standards.

7 Å^{-1} may prove more diagnostic than the region of the $k^3\chi(k)$-spectra >7 Å^{-1} since the higher k region of the spectra tends to be very noisy.

Unique among the XAFS standard spectra were those for the tripeptide glutathione and its components (along with glutamate) glycine and cysteine (Fig. 4). Most notably, cysteine had a significant pre-edge peak in the XANES spectra (arrow Fig. 4) indicating significant orbital mixing (1s → 3d or 1s → 4pz) because of the non-centrosymmetric structure formed when complexed with Ni. Best fits for the Ni cysteine complex were achieved by including both N and S donor ligands in the first shell ($CN_{Ni-S} = 2$ sulfur atoms at $R_{Ni-S} = 2.14$ Å and $CN_{Ni-N} = 2$ nitrogen atoms at $R_{Ni-N} = 1.96$ Å) with C and the oxygen of the hydrating water in the second ($CN_{Ni-C} = 4$ carbon atoms at $R_{Ni-C} = 2.98$ Å and $CN_{Ni-O} = 1.10$ Å oxygen atoms at $R_{Ni-O} = 2.41$ Å). Fits for the Ni–glycine complex indicates that Ni is bound to the amine group and terminal carboxyl groups ($CN_{Ni-N} = 2$ nitrogen atoms at $R_{Ni-O} = 2.04$ Å and $CN_{Ni-O} = 2$ oxygen atoms at $R_{Ni-O} = 2.13$ Å) of two glycine molecules with Ni acting as the bridging atom forming a dimer.

2.3. Ni speciation in A. murale – evidence from X-ray and ATR-FTIR spectroscopy

The numbered spots in the μ-SXRF maps in Fig. 2 correspond to the XANES, $k^3\chi(k)$-spectra and RSF shown in Fig. 5. The dataset included a total of 19 spectra including bulk-EXAFS spectra from extracted sap (#15) and freeze-dried and ground stem (spectra #16 and 18) and leaf tissue (#17 and 19) from soil grown plants. While the spectra are very similar, there are subtleties in each that provide an indication of the Ni coordination. The arrows in Fig. 5a and b point to regions in the XANES and $k^3\chi(k)$-spectra possessing the most diagnostic features. As mentioned previously, the feature in the XANES spectra at about 8.338 keV results from 1s → 3d or 1s → 4pz electronic transitions (i.e., orbital mixing), and is indicative of non-centrosymmetric coordination resulting from either tetrahedral or square pyramidal complexes (Colpas et al., 1991; Feth et al., 2003; Strathmann and Myneni, 2004). In the sample spectra, this feature is small, likely arising from slight distortions in symmetry permitting some p–d orbital mixing which increases the probability of 1s → 3d transitions. The fact that this feature is small and similar to those found in the Ni carboxylic acid and hydrated Ni standard spectra indicates that Ni in the samples has an octahedral geometry.

In some of the spectra (e.g., 1 and 2), there is obvious splitting in the peak around 5.8 Å^{-1} in the $k^3\chi(k)$-spectra which, as was observed while fitting the standards, is indicative of a stronger Ni–ligand complex. The RSF of all spectra show a prominent first shell peak at ~1.6 Å (uncorrected for phase shift) and, in many, another smaller peak at ~2.3 Å (uncorrected for phase shift).

An initial assessment of the coordination environment of Ni in the plant tissues was conducted using conventional NLLSF. Table 1 shows the NLLSF results from fitting the sample spectra using phase

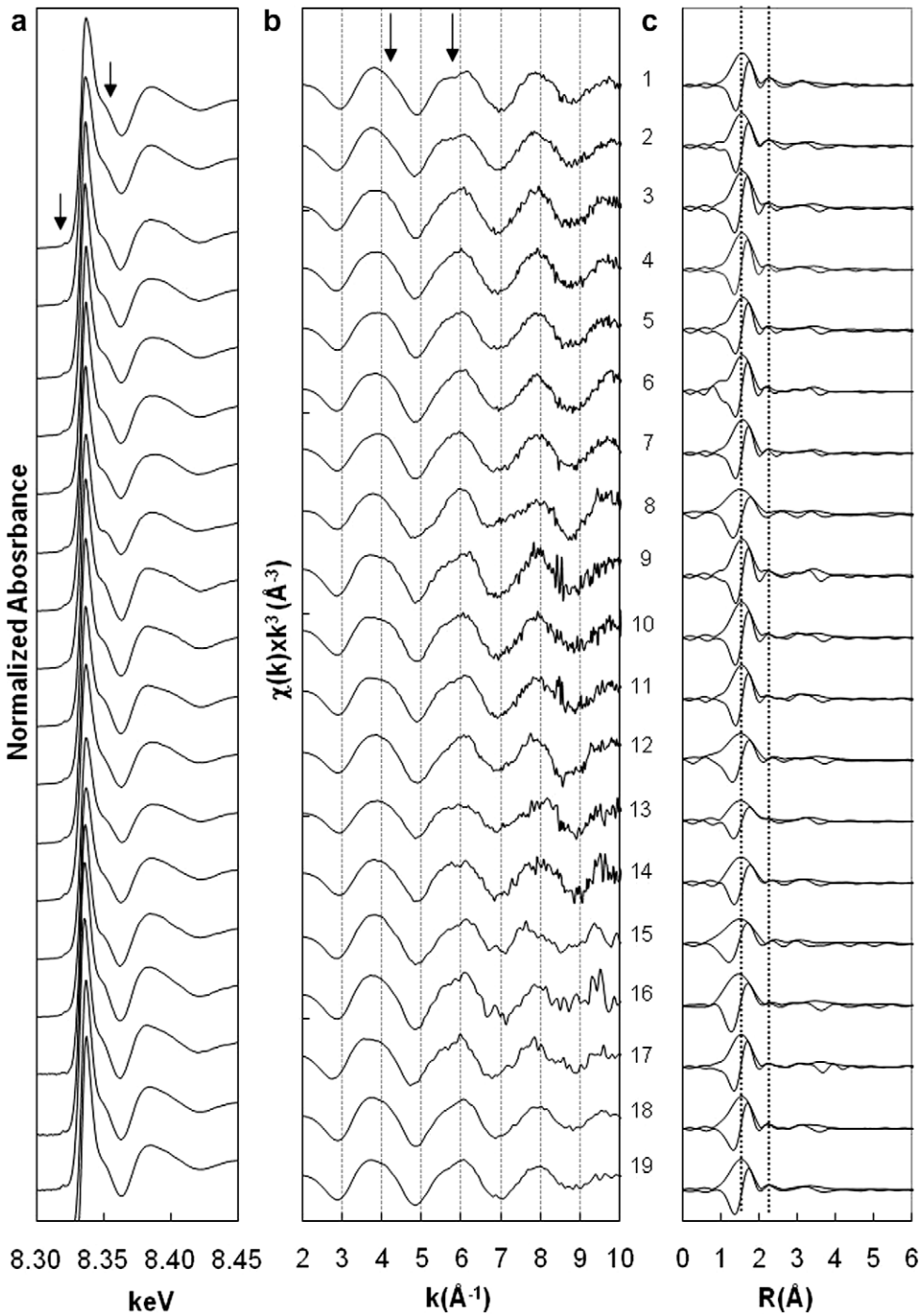

Fig. 5. (a) X-ray absorption near-edge spectra (XANES), (b) $k^3\chi(k)$-spectra and (c) radial structure functions from the points indicated in Fig. 2 throughout several *Alyssum murale* leaves. *Note:* spectra 15 was collected from pressure bomb extracted plant sap and 16–19 were collected from homogenized muck and loam grown, stem and leaf tissues, respectively, and thus are not represented in Fig. 2.

and amplitude functions generated from either $Ni(sal)_2(H_2O)_2$ (Stewart et al., 1961) for Ni–C paths or Ni–imidazole ($(C_3H_4N_2)_6$-$Ni(NO_3)_2$) for Ni–N paths (Santoro et al., 1969). The first coordination shell in all the spectra is occupied by approximately six oxygen/nitrogen atoms at $R_{Ni-O/N} \approx 2.03$–2.06 Å indicating, as was suggested by the small pre-edge feature in the XANES spectra, that the Ni is in an octahedral coordination. Some spectra had a significant second shell contribution from carbon at $R_{Ni-C} = 2.76$–2.91 Å with coordination numbers ranging from CN_{Ni-C} 1.00 to 4.67. It should be noted that second shell coordination numbers less than 2 are outside the error associated with EXAFS spectroscopy second shell coordination number estimates (±40%). However, each of the fits was performed with carbon and without, and carbon was only included when it significantly improved the fit (based on a 20% or greater improvement in the % residual error; X^2_{res} (%)). The NLLSF results show that only oxygen or nitrogen donor ligands participate in the complexation of Ni in the tissues of *A. murale*.

The species contributing to these fitting results were determined by principal component analysis (PCA) using all 19 sample spectra over the k range of 2–10 $Å^{-1}$. The weights of the first four

Table 1
Non-linear and linear least squares fitting results for all micro- and bulk-EXAFS sample spectra.

Non-linear least squares fitting											Linear least squares fitting		
Spectra #	Atom	First shell			Atom	Second shell			ΔE_0 (eV)	X^2_{res} (%)	Ni-organic/amino acid composition	Total (%)	NSS
		CN	R (Å)	$\Delta\sigma^2$ (Å^2)		CN	R (Å)	$\Delta\sigma^2$ (Å^2)					
1	N/O	5.60	2.05	0.005	C	4.67	2.91	0.008	−2.19	3.57	26% Tartrate, 30% histidine, 39% acconitate	95	0.0320
2	N/O	6.30	2.04	0.006	C	3.00	2.89	0.004	−3.56	13.89	27% Tartrate, 29% malate, 34% acconitate	93	0.0509
3	O	6.80	2.05	0.006	C	1.18	2.87	0.001	1.19	2.09	57% Malate, 40% aconitate	97	0.0513
4	O	6.50	2.05	0.005	C	1.50	2.86	0.007	0.59	3.01	52% Malate, 43% aconitate	95	0.0417
5	O	6.75	2.06	0.006	C	1.00	2.81	0.002	2.07	2.74	52% Malate, 35% aconitate	89	0.0455
6	O	6.53	2.05	0.005	C	2.30	2.84	0.009	1.03	6.0S	54% Malate, 52% Ni(aq)	106	0.0484
7	O	6.50	2.05	0.005	C	1.64	2.78	0.005	1.30	4.53	99% Succinate	99	0.0614
8	O	6.07	2.05	0.005	C	–	–	–	1.77	4.98	96% Ni(aq)	96	0.1240
9	O	6.32	2.04	0.004	C	2.30	2.88	0.004	0.44	4.22	101% Malate	101	0.1410
10	O	6.00	2.05	0.005	C	2.70	2.88	0.008	2.38	9.02	92% Malate	92	0.1690
11	O	5.21	2.03	0.005	C	2.58	2.78	0.003	−0.45	8.17	94% Ni(aq)	94	0.1060
12	O	6.20	2.06	0.006	C	2.00	2.83	0.005	1.55	2.83	55% Malate, 38% histidine	93	0.1850
13	O	6.24	2.04	0.004	C	1.50	2.83	0.005	−0.25	5.00	56% Malate, 38% acconitate	94	0.0749
14	O	6.39	2.04	0.005	C	1.93	2.88	0.007	0.64	4.10	93% Malate	93	0.1130
Bulk plant sap (15)	O	4.50	2.03	0.005	C	3.00	2.76	0.005	−0.21	3.30	43% Tartrate, 24% Ni(aq), 23% histidine	86	0.1430
Bulk stem muck (16)	O	6.50	2.03	0.004	C	–	–	–	−2.60	10.19	67% Tartrate, 34% Ni(aq)	101	0.1770
Bulk leaf muck (17)	O	6.00	2.05	0.004	C	2.00	2.84	0.006	−0.09	5.72	67% Succinate, 30% tartrate	97	0.0567
Bulk stem loam (18)	O	6.00	2.04	0.005	C	1.50	2.81	0.009	−0.11	9.27	51% Succinate, 46% tartrate	97	0.0168
Bulk leaf loam (19)	O	6.00	2.04	0.005	C	1.30	2.86	0.004	−0.92	9.95	50% Tartrate, 44% succinate	94	0.0193

CN = coordination number (±20% (Scheidegger et al., 1997)).
R = inter-atomic distance (±0.02 Å for first shell and ±0.05 Å for second shell (Scheidegger et al., 1997)).
$\Delta\sigma^2$ (Å^2) = Debye–Waller factor.
ΔE_0 = phase shift.
X^2_{res} (%) = residual.
NSS = $\sum[k^3\chi(k)_{exp} - k^3\chi(k)_{reconstr.}]^2/\sum[k^3\chi(k)_{exp}]^2$.

components were 140, 21, 18 and 13 with indicator values of 0.0286, 0.0280, 0.0275 and 0.0288, respectively. The total normalized sum square values (a "badness" of fit parameter) significantly improved when going from 2 to 3 components (from 0.0526 to 0.0376), but not four. Therefore, PCA indicates that, while the first component contributes significantly more to the overall fit (i.e., indicating one dominant species), the dataset can best be described by three components. Target transformation (TT) was done using our characterized references to determine the species represented by the abstract principal components. We initially used a reference dataset that included both inorganic and organic standards (see McNear et al. (2007) for entire data set); however, the spoil values for the inorganic standards were large enough (ranging from 6.2 to 25) to exclude them from further consideration. Target transformation indicated that the top three species most likely in our dataset (Table S2 Supplementary data; 2–10 Å^{-1}) are Ni(aq) (2.04), Ni–tartrate (2.43) and Ni–malate (2.73).

Linear least squares fitting (LLSF) of the sample spectra with combinations of the identified references resulted in normalized sum squared values (NSS) ranging from 0.0254 to 0.256 (Table 1). For some of the spectra, linear combinations of tartrate, malate and Ni(aq) alone do not appear sufficient to adequately describe the composition at the sample point, as indicated by high NSS values relative to the average (i.e., NSS > 0.100), and poor fitting of the diagnostic features between 3 and 7 Å^{-1} in the $k^3\chi(k)$-spectra. To optimize the fits, PCA-LLSF was performed using only the 3–7 Å^{-1} region of the $k^3\chi(k)$-spectra. Using this approach, PCA identified Ni–succinate, Ni–aconitate, Ni(aq) and Ni–malate as the primary components (Table S2 Supplementary data; 3–7 Å^{-1}). Unique to the fits over both spectral regions were Ni–malate and Ni(aq), while PCA over the 3–7 Å^{-1} left out Ni–tartrate, but included both Ni–succinate and Ni–aconitate. Including Ni–succinate and Ni–aconitate in the LLSF of the entire spectra resulted in an improvement of the original fits for most of the spectra with the exception of those collected at points 1, 12 and 15 (Fig. 2). Point 1 was collected from a vein of a leaf, point 15 was the bulk-EXAFS spectra collected from the extracted plant sap and point 12 was collected from a non-specific region within a plant leaf. Since points 1 and 15 were collected either from a vein or bulk plant sap, further efforts were made using ATR-FTIR to assess whether Ni in the vasculature of the plant was present in a different chemical form compared to that stored in the bulk of the leaf dermal tissues.

FTIR has been used to investigate a variety of constituents in plants including proteins (Surewicz et al., 1993) and cell wall materials (McCann et al., 1992). No studies, to these authors' knowledge, have used ATR-FTIR methods to characterize plant sap extracts from specialized hyperaccumulating plants. Fig. 6a shows the IR spectra for sap extracted from *A. murale* grown with excess (50 μM) and basal (0.125 μM) amounts of Ni, and Fig. 5b and c the same spectra with malate and histidine reference IR spectra included. In general, because all standards contain one or more carboxyl anions, all of the spectra had two primary absorption bands at ~1640 and 1400 cm^{-1} resulting from carbonyl (νC=O) stretching and C–OH vibrations (νC–OH), respectively. The higher and lower energy of the νC=O and νC–OH bands, respectively, in the sap indicate that in each case (with and without Ni) the carboxylate and alcohol anion of the contributing organic ligands in the plant sap are fully protonated (with Ni or other cations). Of all the standard spectra compared to the sap, histidine shared the most spectral features. Most notably the broad absorption band

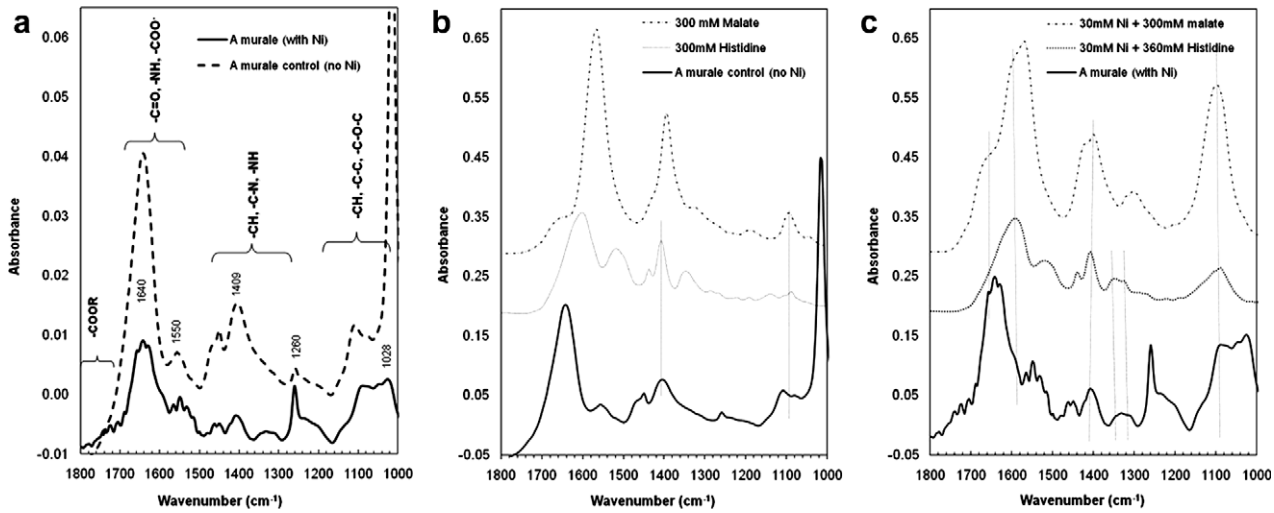

Fig. 6. (a) Near-IR ATR-FTIR spectra of pressure bomb extracted sap from *Alyssum murale* grown with (—) and without (- - -) 50 μM Ni, and near-IR spectra for *A. murale* grown (b) without and (c) with Ni compared to malate and histidine standards.

at 1300–1380 cm^{-1} which was only found in the histidine spectra. Malate is included for comparison because, as was demonstrated earlier, it has consistently been identified using PCA as a component within our sample EXAFS spectral dataset. There are, however, few similarities between the Ni–malate IR standard and the plant saps, lending some support to the hypothesis that Ni is sequestered by a different combination of ligands during transport and for storage.

Based on these findings, all of the sample spectra were re-evaluated using the following criteria: (1) NLLSF parameters, (2) diagnostic features in the XANES spectra, (3) goodness (based on NSS) of the LLSF with particular attention paid to the diagnostic features between 3 and 7 $Å^{-1}$ and (4) ATR-FTIR data. For example, fits with a high NSS value were inspected to determine where the data were inadequately fit, paying particular attention to the diagnostic region between 3 and 7 $Å^{-1}$. In addition, the coordination number and atomic distances for the ligand identified by NLLSF, and the metal species identified by LLSF for the sample spectra were compared to determine if it was appropriate to include the identified ligand in the NLLSF. That is, if the NLLSF indicates that the EXAFS spectra are comprised primarily of histidine, there should be a significant second shell carbon contribution at a slightly longer bond distance in the LLSF of that spectra, as well as splitting in the $k^3\chi(k)$-spectra at ~5.8 $Å^{-1}$ and broadening of the maximum absorption peak in the XANES spectra.

The LLSF results from using these revised fitting criteria can be found in Table 1. The average distribution of Ni species within all of the sample spectra was found to be 34% Ni–malate, 16% Ni(aq), 15% Ni–tartrate, 14% Ni–succinate, 12% Ni–aconitate and 5% Ni histidine. The inclusion of Ni–succinate and Ni–aconitate was found to significantly improve the fit for some of the spectra. We interpret this improvement in the fit to indicate the presence of a weakly complexing donor ligand instead of solely the hydrated Ni species. Keeping with this interpretation, 55% of the Ni in the plant tissues appears to be complexed by stronger ligands (malate, histidine and tartrate), with the remaining 42% as either weak complexes with non-specific oxygen donor ligands (e.g., succinate, aconitate) or possibly counter-ions (e.g., sulfate). Spectra taken from leaf veins and sap contribute most to the histidine complexed Ni fraction. Fits from the bulk-EXAFS spectra of leaves and stems from plants grown in Ni enriched soils (*Fig.* S1; Supplemental data) show a similar trend in that 30–67% of the Ni is complexed with tartrate and the balance with succinate and/or counter-ions.

3. Discussion

Determination of metal speciation in plant tissues is difficult due to the complex and dynamic matrix within which they reside. Identification of ligands responsible for metal detoxification in hyperaccumulating plants using solely chromatographic methods are limited by the typically low recovery of metals from the tissue extractions, the inability to specify which cellular compartments the complex comes from (e.g., vacuole vs vasculature), as well as potential mixing, degradation or transformation of the cellular components once extracted. Direct measures of metal speciation in plant tissues using spectroscopic methods may overcome some of these limitations, but they too have their drawbacks. Using solely hard X-ray spectroscopic methods to directly speciate metals in biological tissues is complicated because the ligands often associated with the metals are comprised of weak backscattering atoms (e.g., C) which provide very little structure to the EXAFS spectra. In this paper, we have attempted to overcome many of these concerns by combining multiple analytical techniques and statistical data fitting methods to ascertain the speciation and distribution of Ni within *A. murale*.

Using electron microscopy and μ-SXRF we found that Ni is evenly distributed throughout the epidermal tissues, entrained in xylem vesicles, and absent from the mesophyll of the leaf. There is no clear correlation of Ni with any of the other elements analyzed. Sulfur was found to be concentrated in the mesophyll where it has been shown to have a functional role in several metabolic processes. The majority of sulfur is stored in a plant as the inorganic anion sulfate with the remainder incorporated into organic forms such as proteins, chloroplast lipids, or secondary metabolites (Marschner, 1995). Sulfur is a key constituent, both structural and functional, in proteins, namely cysteine, and the strong antioxidant glutathione. Many of the functions requiring S take place in chloroplasts of photosynthetically active tissues of the plant and thus it is not surprising that the S content of these tissues would be elevated. Kupper et al. (2001) and Broadhurst et al. (2004) both found Ni to be associated with sulfur in the plant epidermal cell vacuoles in *A. lesbiacum*, *A. bertolonii* and *A. murale*, which is opposite to the pattern we observed. They concluded that the excess sulfur was probably sulfate acting as a counter-ion to Ni, and possibly an inorganic nickel sulfate species stored in the epidermal vacuoles. In the Kupper et al. (2001) study, the excess Ni treatments were supplied to the plants as $NiSO_4$ (up to 4000 mg/kg) which may have induced the observed Ni–S associations. Sulfate can be directly taken up

Please cite this article in press as: McNear, D.H., et al. The hyperaccumulator *Alyssum murale* uses complexation with nitrogen and oxygen donor ligands for Ni transport and storage. Phytochemistry (2009), doi:10.1016/j.phytochem.2009.10.023

from the growth solution and, if not used for other plant functions, the excess stored in the cell vacuole (Lombi et al., 2002). However, Broadhurst et al. (2004) noted in their studies that regardless of the sulfate concentration and type of Ni supplied (i.e., $NiSO_4$ vs $Ni\text{-}C_4H_6O_4$), S concentration in the leaves (on a total S basis) was still elevated. Tappero et al. (2007) also found elevated shoot S concentrations in *A. murale* grown in mixed metal (Ni + Co, Ni + Zn and Ni + Co + Zn) hydroponic solutions noting that in the Co treated plants (Ni + Co, Ni + Co + Zn) the S content significantly increased compared to the Ni only treatment and, based on the SXRF maps, was correlated with Co. Their study suggests that the mechanisms used by *A. murale* to detoxify Ni are different than those used for Co, for which S may play a role. Ingle et al. (2005) found that at Ni concentrations high enough to support Ni hyperaccumulation (i.e., 0.03 mM $NiSO_4$) there were no S-metabolism-related genes upregulated; however, when moderately high Ni was added (0.3 mM $NiSO_4$), genes responsible for S-metabolism were upregulated. This only highlights the point that even metal hyperaccumulating plants that have evolved the ability to tolerate high metal concentrations have an upper threshold beyond which inducible chemical stress responses are upregulated. In the current study, these solution concentrations were not exceeded.

Our analyses indicated that more often than not Ni within *A. murale* is complexed with malate or tartrate, with the remaining fractions existing either as weak complexes with non-specific oxygen donor ligands, or as complexes with counter-ions. The consistent statistical identification of tartrate in many of the sample spectra (particularly freeze-dried and ground tissues) is surprising as few studies investigating Ni hyperaccumulation in Mediterranean *Alyssum* species have demonstrated an obvious role for tartrate in metal hyperaccumulation, more often malic or citric acids are implicated. Tartrate has been found, however, in other hyperaccumulating species. In *Solanum nigrum* plants exposed to elevated Cd, tartrate was found to be the second most abundant organic acid after acetic acid in young leaves, followed by malic acid (an order that was reversed after plant maturity) (Sun et al., 2006). Callahan et al. (2008), using LC–MS and GC–MS, also identified Ni–tartrate in latex from the Ni hyperaccumulating tree *Sebertia acuminate* (along with citric and malic acids). In addition to identifying a new Ni–ligand, they also noted that citric acid concentrations were not sufficient enough to satisfy the necessary charge balance with Ni and, more than likely, tartrate and malate were fulfilling this role. The nickel stability constant for malate (Ni–malate $pK = 3.2$) is similar to that of tartrate (Ni–tartrate $pK = 3.2$) but much lower than that of citrate (Ni–citrate $pK = 5.2$) indicating that if citrate was around it would be the dominant ligand for Ni followed by malate and/or tartrate. Attempts were made to re-fit the sample spectra using citrate instead of tartrate, but these always resulted in a much poorer fit. It is possible that even with the robust fitting procedures used in this study, the subtle differences between Ni–citrate and Ni–tartrate (each having similar NLLSF parameters and $k^3\chi(k)$-spectra) along with the data quality of the standards and samples may have resulted in some fitting error. Nevertheless, the statistical and analytical analyses used in this study indicate that tartrate is playing a role in Ni sequestration in *A. murale*. In addition to malate, malonate has been implicated in the complexation of Ni in several Ni hyperaccumulating *Alyssum* species including *A. bertolonii* (Pelosi et al., 1976) and *A. serpyllifolium* (Brooks et al., 1981). Boominathan and Doran (2003), Tolra et al. (1996), and Shen et al. (1997) found organic acid concentrations to be endogenously higher in several hyperaccumulating plants, finding no specific response (i.e., increased OA production) when the plants were exposed to metals. They all noted that the constitutively high organic acid concentrations were enough to complex the increased Ni concentrations in the plants tested.

In addition to organic acids, we also found evidence of Ni–histidine complexes in leaf veins and pressure-bomb extracts. Kramer et al. (1996) showed that exposure of *A. lesbiacum* to 0.3 mM Ni in hydroponic cultures resulted in a 36-fold increase in xylem histidine levels implying that histidine plays a key role in the transport of Ni from the roots to the shoots. Ostergren et al. (1999) showed that transcript levels for the first enzyme in the biosynthetic pathway of histidine, ATP–phosphoribosyltransferase (ATP–PRT), were constitutively higher in the Ni hyperaccumulator *A. lesbiacum* when exposed to elevated Ni. They found overexpression of an ATP–PRT cDNA in *A. thaliana* resulted in an increase in the levels of histidine in the shoots and a concomitant increase in Ni tolerance, but no increase in Ni accumulation. Kerkeb and Kramer (2003) showed that Ni was taken up by *A. lesbiacum* as the free hydrated ion and that the constitutively higher histidine concentration in the roots was important for the loading of Ni from the roots into the xylem; a process they determined to be interdependent. It should be noted, however, in their study there was a leveling off and an eventual decline in xylem histidine concentrations after approximately 11 h of Ni exposure (see Fig. 1 Kerkeb and Kramer (2003)). This may indicate that while histidine is important in the delivery of Ni to the xylem from the roots, and some histidine may concurrently be released into the xylem, other ligands or counter-ions will be necessary to balance the molar excess of Ni. The results in this study are in agreement with this interpretation, and supports a model where transport in the xylem is facilitated by chelation of Ni in some part by histidine and other non-specific organic acids, after which it is delivered from the leaf veins to the vacuoles of the leaf epidermal cells where it is stored complexed with organic acids (most notably malate) or with less specific ligands (e.g., aconitate, succinate) or counter-ions (e.g., sulfate).

4. Conclusions

The findings contained herein contribute to the current understanding of metal tolerance and hyperaccumulation and provide an example of how coupling complementary techniques at multiple scales can provide a unique picture of metal sequestration and compartmentalization in biological tissues. While this study contributes to the growing evidence for the importance of organic/amino acids and counter-ions in the transport and storage of metals, there are still many questions to be answered regarding metal uptake, delivery and storage in hyperaccumulating plants. Little is known about the physiological, biochemical and genetic mechanisms involved in metal uptake from the rhizosphere, transport through the vasculature and preferential offloading of metals into cellular compartments within leaf and stem tissues (e.g., epidermal vacuoles, trichome basal compartments). Understanding these mechanisms will not only satiate our curiosity as to the fundamental evolutionary and ecological processes that guided these plants to the hyperaccumulation phenotype, but they will also help in efforts to improve food crop production via, for example, biofortification or improved pathogen resistance. The results obtained and methods used in this study should assist in these efforts.

5. Experimental

5.1. A. murale propagation

The 'Kotodesh' accession of the Ni hyperacumlator *A. murale* (Waldst. & Kit.) was grown in a glass house in nickel enriched soils collected from an area adjacent to an historic Ni refinery in Port Colborne, Ontario, Canada. The speciation of Ni in these soils and the soil physicochemical characteristics have been described

elsewhere (Kukier and Chaney, 2001; McNear et al., 2005). Soils were sieved wet, mixed thoroughly and 1.5 kg (dry weight) of loam soil or 0.8 kg (dry weight) of muck soil were placed in 1.5 l plastic pots. Based on Mehlich III soil test analyses, the total amounts of macro- and micro-nutrients applied to each pot were: 154 mg N (as calcium nitrate), 291 mg P (as calcium phosphate and potassium phosphate), 231 mg K (as potassium phosphate), 22 mg Mg (as magnesium sulfate) and 1 mg B (as boric acid) (Siebielec et al., 2007). All fertilizers were added as solutions with the exception of calcium phosphate, which was added as a dry powder. A previous study has shown that Port Colborne soils can develop a Mn deficiency, particularly when limed to alleviate Ni phytotoxicity (Kukier and Chaney, 2001). Therefore, $MnSO_4$ was added at a rate of 200 kg Mn/h to each pot (Siebielec and Chaney, 2006). The fertilizers were mixed with the soil in plastic bags and added to the pots. The pots were watered and incubated for 7 days after which the soils were mixed again and cultivated. Pots were watered as needed using reverse osmosis filtered H_2O and saucers were used to prevent loss of leachate. Control plants were grown in soils from the same region but without Ni enrichment. Some plants were grown in the greenhouse aeroponically in a General Hydroponics Clone Machine 20 (General Hydroponics, Sebastopol, CA) using modified 1/4 strength Hoagland's with Fe(III)–HBED (*N*,*N*′-di-(2-hydroxybenzoyl)-ethylenediamine-*N*,*N*′-diacetic acid) to avoid metal chelator interactions (Chaney, 1988). Control plants were grown in solutions containing 0.125 μM Ni while elevated treatments had 50 μM Ni (added as $Ni(NO_3)_2$). Both soil and aeroponically grown plants received light for 16 h each day using a combination of high pressure sodium vapor lamps and natural sunlight. Day/night temperatures were approximately 25 and 21 °C, respectively.

5.2. Electron probe micro-analysis (EPMA)

Plant samples were prepared by immersing whole sections of shoot in liq. N_2 after which they were dried under vacuum at −80 °C for 24 h to prevent ice crystal formation. Leaves were then fractured to expose the interior of the leaf and pieces were placed on end on a carbon stub. Prior to analysis the samples were sputter-coated with carbon and then examined on a JOEL JXA-8600 microprobe (John Hopkins University) with wavelength and energy dispersive detectors (WDS and EDS, respectively). Samples were first scanned manually from 50 to 300× using background scattered electron (BSE) imaging to find regions of high Ni concentration after which EDS was used to generate elemental maps for O, K, Ca, Fe, Al and Ni.

5.3. ATR-FTIR standard and plant sap characterization

Attenuated total reflectance-Fourier transform infrared (FTIR) spectroscopy was employed to characterize the organic and amino acid standards used in EXAFS PCA-LLSF, as well as in characterization of extracted xylem sap from *A. murale*. Plant sap was collected from hydroponically grown *A. murale* plants by inserting cut sections of shoots into a pressure bomb apparatus (Soil Moisture Equip. Corp., Goleta, CA), adjusting the pressure to ∼15 bar and using a hypodermic needle to extract the sap (∼1 mL) as it exuded from the cut stem over a 1 h period. A Thermo Electron NEXUS 670 FTIR spectrometer equipped with a PIKE Technologies horizontal attenuated total reflectance (HATR) flow-through accessory and a germanium (Ge) internal reflection element was used for data collection. The organic acids citrate, malate, malonate, oxalate, tartrate, aconitate, and the amino acids histidine, cysteine and glycine were examined with and without Ni present to verify the type of complex formed. Standards in the concentrations detailed below and extracted sap were pipetted directly onto the germanium crystal prior to analysis.

5.4. EXAFS spectroscopy standard preparation, data collection and characterization

A total of 12 aqueous organic standards were prepared as follows: Ni–aqueous, 30 mM $Ni(NO_3^-)_2$; Ni–aconitate, 50 mM $Ni(NO_3^-)_2$ + 150 mM aconitate; Ni–malate, 30 mM $Ni(NO_3^-)_2$ + 300 mM malate; Ni–malonate, 30 mM $Ni(NO_3^-)_2$ + 300 mM malonate; Ni–citrate, 30 mM $Ni(NO_3^-)_2$ + 120 mM citrate; Ni–oxalate, 30 mM $Ni(NO_3^-)_2$ + 300 mM oxalate; Ni–tartrate, 50 mM $Ni(NO_3^-)_2$ + 500 mM tartrate; Ni–succinate, 30 mM $Ni(NO_3^-)_2$ + 150 mM succinate; Ni–histidine, 30 mM $Ni(NO_3^-)_2$ + 300 mM histidine; Ni–glutathione, 30 mM $Ni(NO_3^-)_2$ + 300 mM glutathione; Ni–cysteine, 30 mM $Ni(NO_3^-)_2$ + 300 mM cysteine; Ni–glycine, 30 mM $Ni(NO_3^-)_2$ + 300 mM glycine. ACS trace metal grade chemicals, acid washed containers and ultra-pure double-deionized (18.2 Ω Millipore) water were used to generate all standards. The pH was adjusted using trace metal grade nitric acid (HNO_3) or potassium hydroxide (KOH).

XAS data for standards were collected on beamline X-11A at the National Synchrotron Light Source (NSLS), Brookhaven National Laboratory, Upton, NY (unless otherwise stated). The electron beam energy was 2.5–2.8 GeV with a maximum beam current of 300 mA. The monochromator consists of two parallel Si(1 1 1) crystals with a vertical entrance slit opening of ∼0.5 mm. The beam size on the sample was maintained at 2 × 10 mm for all samples and standards. Prior to data collection, the energy was calibrated to the first inflection point on the K adsorption edge of a Ni metal foil standard (E_0 = 8.333 keV for Ni). Aqueous standards were loaded into individual acrylic sample holders and sealed with Kapton™ tape. A non-adhesive Kapton™ film was placed on the adhesive side of the tape where it covered the sample reservoir to avoid any interaction of the sample with the tape adhesive. The samples were then mounted 45° to the incident beam and data collected at the Ni K-edge over the energy range 8183–9082 eV in fluorescence mode using a N_2/Ar (95/5%) filled Lytle Cell. To optimize the Ni signal and remove elastically scattered radiation, the fluorescence signal was filtered using a Co foil, one to two sheets of aluminum foil and Soller slits. Harmonic rejection was achieved by detuning the monochromator 20% of I_0. Multiple scans ($\geqslant$3) were collected for each sample to improve the signal-to-noise ratio.

EXAFS spectroscopy data analyses were performed using WinXAS 3.1 (Ressler, 1997). Prior to averaging, the individual spectra were background corrected and normalized. Background subtraction was performed by fitting a linear polynomial to the pre-edge region between 150 and 50 eV below the Ni K-edge. The edge jump was normalized to unity by fitting a linear polynomial between 100 and 500 eV above the Ni K-edge. The threshold energy (E_0) was determined by selecting the root of the second derivative through the absorption edge of the differentiated spectra, and used to convert the spectra from energy to *k*-space (photoelectron wave vector ($Å^{-1}$)). A cubic spline function with $\leqslant$7 knots was then used to remove the contribution to the spectrum resulting from atomic absorption in the absence of backscattering contributions. This step generated the EXAFS function ($\chi(k)$), which was then weighted by k^3, to compensate for dampening of the EXAFS amplitude with increasing *k*. The $k^3\chi(k)$-spectra were then Fourier transformed using a Bessel window with a smoothing parameter of 3–4 to reduce artifacts due to the finite Fourier filtering range used. This step produced radial structural functions (RSF) which were not corrected for phase shift.

The first two major shells below 3.5 $Å^{-1}$ were individually selected, back-transformed, and fit using a non-linear least squares fitting (NLLSF) approach and theoretical scattering paths generated using ATOMS and FEFF 7.02 software packages (Zabinsky et al.,

1995). The Ni–O and Ni–C (organic acids) phase and amplitude functions were generated using either nickel acetate tetrahydrate ($(Ni(CH)_3COO)_2 \cdot H_2O$) (Nicolai et al., 1998) or diagua-bis(salicylaldehydato) nickel ($(Ni(sal)_2(H_2O)_2)$) (Stewart et al., 1961) and Ni–N (amino acids) paths using Ni–imidazole ($(C_3H_4N_2)_6Ni(NO_3)_2$) (Santoro et al., 1969). The Ni–N, Ni–S, N–C and Ni–O phase and amplitude functions for fitting the cysteine standard were generated using $K_2(Ni(cys)_2)$ (Leung et al., 2008). The parameters obtained fitting the individual shells were then refined using a multi-shell fit over the entire spectra in k and R spaces. The energy shift parameters (E_0) were set equal for all paths and the root mean square disorders (RMSD (σ^2 (Å^2)) or the Debye–Waller factor) and bond distance (R) were set equal for those metals sharing atomic shells. The amplitude reduction factor (S_0^2) was fixed at 0.85. The number of variables used in the fits were always less than the number of independent points (NIP) calculated as $N_{pts} = 2\Delta k \Delta R/\pi$. Errors in the bond distance (R) are estimated to be $R \pm 0.02$ Å and $R \pm 0.05$ Å, and errors for the coordination number (CN) are estimated to be CN ± 20% and CN ± 40%, for the first (Ni–O/S/N) and second shells (Ni–Ni//C), respectively. These estimates are based on the fitting results provided by WinXAS and comparison with previously published XRD and EXAFS spectroscopy data on similar systems (O'Day et al., 1994).

5.5. μ-SXRF and μ-EXAFS spectroscopy's data collection and analysis

Micro-EXAFS and μ-synchrotron X-ray fluorescence (μ-SXRF) data were collected on beamline 10.3.2 (1.9 GeV and 300 mA) at the Advanced Light Source, Lawrence Berkeley National Lab (Berkeley, CA). Leaves and stems were removed from living plants and mounted directly to a Peltier cold stage using metal-free silicon vacuum grease and rapidly frozen to ~−30 °C. The sample stage was then oriented 45° to the incident X-ray beam. Fluorescence signals were collected using a Ge solid-state multi-element detector. To assess the spatial distribution of Ni and other elements in the samples, fluorescence maps were collected over 1000 μm^2 (coarse map) and 200 μm^2 (fine map) with a beam size of 16 × 7 and 5 × 5 μm, respectively, using a step size of 20 and 5 μm and an integration time of 100 ms. For mapping, the beam energy was set to 11 keV to allow the detection of Ni, Fe, Ca, Co, Cu, Zn, and Mn. To determine the Ni speciation at regions of interest in the maps, μ-XAS spectra were collected up to 500 eV above the Ni K-edge. Prior to μ-XAS data collection, the beamline energy was calibrated to the first inflection point of the Ni metal foil standard (E_0 = 8.333 keV).

Analysis of the EXAFS spectra was done using both NLLSF as was described above for fitting the standards and principal component analysis linear least squares fitting (PCA-LLSF). Traditional shell fitting was used as an initial assessment of the coordination environment of Ni with particular focus on the second shell coordination number as an indication of the relative strength of the complex. PCA-LLSF was then performed using Labview™ based data analysis software developed by 10.3.2 beamline scientists (available for free download at their website; http://xraysweb.lbl.gov/uxas/Beamline/Software/Software.htm), to identify and quantify the Ni–ligand complexes contributing to the spectra. Both of these fitting procedures were chosen because analysis of EXAFS spectra collected from multicomponent systems (such as plants) cannot rely on traditional fitting procedures alone in which atomic shells are individually selected and fit. The difficulty arises because multiple species in the system may have overlapping atomic shells making it difficult if not impossible to separate each of them out. Therefore, to determine the species present within a mixed system, a dataset of spectra from multiple spots throughout a sample are analyzed statistically using principal component analysis (PCA) (Wasserman et al., 1999). The PCA technique determines if the data set can be described as weighted sums of a smaller number of components, which would be the case if each spot in the dataset is comprised of a smaller number of distinct compounds. Selection of the number of principal components was made where the empirical indicator (IND) and Eigenvalues were at their minimum (Malinowski, 1977). Target transformation (TT) was then used to identify the components by taking a spectrum of a known reference compound and mathematically removing from the spectrum anything that did not look like principal components identified by PCA. If minimal information is removed from the known reference spectrum, then it is most likely present in the sample. Reference spectra are evaluated for their "goodness of fit" by the SPOIL value (Malinowski, 1978). Generally, numbers <1.5 are considered excellent, 1.5–3 good, 3–4.5 fair, 4.5–6 poor and >6 unacceptable. After the contributing standard phases are identified, linear least squares fitting (LLSF) is used to determine the amount (%) of each standard within the individual sample spectra making up the dataset. The fit is optimized where the normalized sum squared ($NSS = \sum[k^3\chi(k)_{exp} - k^3\chi(k)_{reconstr.}]^2/\sum[k^3\chi(k)_{exp}]^2$) value is at a minimum. A reference phase was included in the fit only if it decreased the NSS by 20% or more. The accuracy of this fitting approach is dependent upon the data quality, the completeness of the standards data set, and the range over which the data were fit (Manceau et al., 2002).

Acknowledgements

The authors would like to thank Dr. Ken Livi of the Department of Earth and Planetary Sciences at Johns Hopkins University for help with EMPA data collection, analysis and interpretation. We thank Dr. Kirk Czymeck of the Delaware Biotechnology Institute for help collecting the confocal and SEM image of leaf cross-sections. We thank Dr. Ryan Tappero for assistance/instruction with plant propagation and Dr. Mike Borda for help with collecting ATR-FTIR spectra. We thank Dr. Timothy Strathman for providing EXAFS spectra for selected Ni-organic acid standards. We thank Matthew Marcus for assistance with μ-EXAFS data collection at the Advanced Light Source (ALS) beamline 10.3.2 and the staff of beamline X11A at the National Synchrotron Light Source (NSLS) for their assistance in the collection of EXAFS standards spectra. The Advanced Light Source is supported by the Office of Science, Basic Energy Sciences, Division of Materials Science of the US Department of Energy under Contract No. DE-AC02-05CH11231. Use of the National Synchrotron Light Source, Brookhaven National Laboratory, was supported by the US Department of Energy, Office of Science, Office of Basic Energy Sciences, under Contract No. DE-AC02-98CH10886.

Appendix A. Supplementary data

Supplementary data associated with this article can be found, in the online version, at doi:10.1016/j.phytochem.2009.10.023.

References

Assuncao, A.G.L., Bookum, W.M., Nelissen, H.J.M., Vooijs, R., Schat, H., Ernst, W.H.O., 2003. Differential metal-specific tolerance and accumulation patterns among *Thlaspi caerulescens* populations originating from different soil types. New Phytol. 159, 411–419.

Boominathan, R., Doran, P.M., 2003. Organic acid complexation, heavy metal distribution and the effect of ATPase inhibition in hairy roots of hyperaccumulator plant species. J. Biotechnol. 101, 131–146.

Boyd, R.S., Martens, S.N., 1998. Nickel hyperaccumulation by *Thlaspi montanum* var. montanum (Brassicaceae): a constitutive trait. Am. J. Bot. 85, 259.

Broadhurst, C.L., Chaney, R.L., Angle, J.S., Erbe, E.F., Maugel, T.K., 2004a. Nickel localization and response to increasing Ni soil levels in leaves of the Ni hyperaccumulator *Alyssum murale*. Plant Soil 265, 225–242.

Broadhurst, C.L., Chaney, R.L., Angle, J.S., Maugel, T.K., Erbe, E.F., Murphy, C.A., 2004b. Simultaneous hyperaccumulation of nickel, manganese, and calcium in *Alyssum* leaf trichomes. Environ. Sci. Technol. 38, 5797–5802.

Broadhurst, C.L., Tappero, R.V., Maugel, T.K., Erbe, E.F., Sparks, D.L., Chaney, R.L., 2009. Interaction of nickel and manganese in accumulation and localization in leaves of the Ni hyperaccumulators *Alyssum murale* and *Alyssum corsicum*. Plant Soil 314, 35–48.

Brooks, R.R., Shaw, S., Marfil, A.A., 1981. The chemical form and physiological-function of nickel in some Iberian *Alyssum* species. Physiol. Plant. 51, 167–170.

Cabaniss, S.E., McVey, I.F., 1995. Aqueous infrared carboxylate absorbances: aliphatic monocarboxylates. Spectrochim. Acta, Part A 51, 2385–2395.

Cabaniss, S.E., Leenheer, J.A., McVey, I.F., 1998. Aqueous infrared carboxylate absorbances: aliphatic di-acids. Spectrochim. Acta, Part A 54, 449–458.

Callahan, D.L., Roessner, U., Dumontet, V., Perrier, N., Wedd, A.G., O'Hair, R.A.J., Baker, A.J.M., Kolev, S.D., 2008. LC–MS and GC–MS metabolite profiling of nickel(II) complexes in the latex of the nickel-hyperaccumulator tree *Sebertia acuminate* and identification of mehtylated alderic acid as a new nickel(II) ligand. Phytochemistry 69, 240–251.

Chaney, R.L., 1988. Plants can utilize iron from Fe–*N*,*N*′-di-(2-hydroxybenzoyl)-ethylenediamine-*N*,*N*′-diacetic acid, a ferric chelate with 106 greater formation constant than Fe–EDDHA. J. Plant Nutr. 11, 1033–1050.

Colpas, G.J., Maroney, M.J., Bagyinka, C., Kumar, M., Willis, W.S., Suib, S.L., Baidya, N., Mascharak, P.K., 1991. X-ray spectroscopic studies of nickel complexes with application to the structure of nickel sites in hydrogenases. Inorg. Chem. 30, 920–928.

Dobson, K.D., McQuillan, A.J., 1999. In situ infrared spectroscopic analysis of the adsorption of aliphatic carboxylic acids to TiO_2, ZrO_2, Al_2 O_3 and Ta_2 O_5 from aqueous solutions. Spectrochim. Acta, Part A 55, 1395–1405.

Ebbs, S., Lau, I., Ahner, B., Kochian, L., 2002. Phytochelatin synthesis is not responsible for Cd tolerance in the Zn/Cd hyperaccumulator *Thlaspi caerulescenes* (J. and C. Presl). Planta 214, 635–640.

Feth, M.P., Klein, A., Bertagnolli, H., 2003. Investigation of the ligand exchange behavior of square planar nickel(II) complexes by X-ray absorption spectroscopy and X-ray diffraction. Eur. J. Inorg. Chem. 5, 839–852.

Ingle, R.A., Smith, J.A.C., Sweetlove, L.J., 2005. Responses to nickel in the proteome of the hyperaccumulator plant *Alyssum lesbiacum*. Biometals 18, 627–641.

Kerkeb, L., Kramer, U., 2003. The role of free histidine in xylem loading of nickel in *Alyssum lesbiacum* and *Brassica juncea*. Plant Physiol. 131 (2), 716–724.

Kramer, U., Cotter-Howells, J.D., Charnock, J.M., Baker, A.J.M., Smith, J.A.C., 1996. Free histidine as a metal chelator in plants that accumulate nickel. Nature 379, 635–638.

Kukier, U., Chaney, R.L., 2001. Amelioration of nickel phytotoxicity in muck and mineral soils. J. Environ. Qual. 30, 1949–1960.

Kupper, H., Lombi, E., Zhao, F.J., Wieshammer, G., McGrath, S.P., 2001. Cellular compartmentation of nickel in the hyperaccumulators *Alyssum lesbiacum*, *Alyssum bertolonii* and *Thlaspi goesingense*. J. Exp. Bot. 52, 2291–2300.

Kupper, H., Mijovilovich, A., Meyer-Klaucke, W., Kroneck, P.M.H., 2004. Tissue- and age-dependent differences in the complexation of cadmium and zinc in the cadmium/zinc hyperaccumulator *Thlaspi caerulescens* (Ganges ecotype) revealed by X-ray absorption spectroscopy. Plant Physiol. 134, 748–757.

Leung, B.O., Jalilevand, F., Szilagyi, R.K., 2008. Electronic structure of transition metal–cysteine complexes from X-ray absorption spectroscopy. J. Phys. Chem. B 112, 4770–4778.

Lombi, E., Tearall, K.L., Howarth, J.R., Zhao, F.J., Hawkesford, M.J., McGrath, S.P., 2002. Influence of iron status on cadmium and zinc uptake by different ecotypes of the hyperaccumulator *Thlaspi caerulescens*. Plant Physiol. 128, 1359–1367.

Malinowski, E.R., 1977. Determination of the number of factors and the experimental error in a data matrix. Anal. Chim. Acta 49, 612–617.

Malinowski, E.R., 1978. Theory of error for target factor analysis with applications to mass spectrometry and nuclear magnetic resonance spectrometry. Anal. Chim. Acta 103, 354–359.

Manceau, A., Marcus, M.A., Tamura, N., 2002. Quantitative speciation of heavy metals in soils and sediments by synchrotron X-ray techniques. In: Fenter, P.A., Rivers, M.L., Sturchio, N.C., Sutton, S.R. (Eds.), Applications of Synchrotron Radiation in Low-temperature Geochemistry and Environmental Sciences, Reviews in Mineralogy and Geochemistry, vol. 49. Mineral. Soc. Amer., pp. 341–428.

Marschner, H., 1995. Mineral Nutrition of Higher Plants. Academic Press, San Diego, CA, USA.

McCann, M.C., Hammouri, M., Wilson, R., Belton, P., Roberts, K., 1992. Fourier transform infrared microspectroscopy is a new way to look at plant cell wall. Plant Physiol. 100, 1940–1947.

McNear, D.H., Peltier, E., Everhart, J., Chaney, R.L., Sutton, S.R., Newville, M., Rivers, M., Sparks, D.L., 2005. Application of quantitative fluorescence and absorption-edge computed microtomography to image metal compartmentalization in *Alyssum murale*. Environ. Sci. Technol. 39, 2210–2218.

McNear, D.H., Chaney, R.L., Sparks, D.L., 2007. The effects of soil type and chemical treatment on nickel speciation in refinery enriched soils: a multi-technique investigation. Geochim. Cosmochim. Acta 71, 2190–2208.

Montargès-Pelletier, E., Chardot, V., Echevarria, G., Michot, L.J., Bauer, A., Morel, J.-L., 2008. Identification of nickel chelators in three hyperaccumulating plants: an X-ray spectroscopic study. Phytochemistry 69, 1695–1709.

Nicolai, B., Kearley, G.J., Johnson, M.R., Fillaux, F., Suard, E., 1998. Crystal structure and low-temperature methyl-group dynamics of cobalt and nickel acetates. J. Chem. Phys. 109, 9062–9074.

O'Day, P.P., Reher, J.J., Zabinsky, S.I., Brown Jr., G.E., 1994. Extended X-ray absorption fine structure (EXAFS) analysis of disorder and multiple-scattering in complex crystalline solids. J. Am. Chem. Soc. 116, 2938–2949.

Ostergren, J.D., Brown Jr., G.E., Parks, G.A., Tingle, T.N., 1999. Quantitative speciation of lead in selected mine tailings from Leadville, CO. Environ. Sci. Technol. 33, 1627–1636.

Pawlukojc, A., Leciejewicz, J., Ramirez-Cuesta, A., Nowicka-Scheibe, J., 2005. L-cysteine: Neutron spectroscopy, Raman, IR and ab initio study. Spectrochim. Acta A 61, 2474–2481.

Pelosi, P., Fiorentini, R., Galoppini, C., 1976. On the nature of nickel compounds in *Alyssum bertolonii*. Agric. Biol. Chem. 40, 1641–1642.

Ramos, J.M., Grisset, F.O., Felcman, J., Claudio, A.T.S., 2008. Fourier transform infrared and Raman spectra, and AB initio calculations for cadmium(II)-cysteinate glycinate complex [Cd(Cys)(Gly)]. Spectrochim. Acta A 71, 1364–1370.

Ressler, T., 1997. WinXAS: a new software package not only for the analysis of energy-dispersive XAS data. J. Phys. IV 7, 269–270.

Santoro, A., Mighell, A.D., Zocchi, M., Reimann, C.W., 1969. The crystal and molecular structure of hexakis(imidazole)nickel(II) nitrate, $(C_3H_4N_2)_6Ni(NO_3)_2$. Acta Crystallogr. Sect. B: Struct. Sci. 25, 842–847.

Sarret, G., Saumitou-Laprade, P., Bert, V., Proux, O., Hazemann, J.L., Traverse, A.S., Marcus, M.A., Manceau, A., 2002. Forms of zinc accumulated in the hyperaccumulator *Arabidopsis halleri*. Plant Physiol. 130, 1815–1826.

Schat, H., Llugany, M., Vooijs, R., Hartley-Whitaker, J., Bleeker, P.M., 2002. The role of phytochelatins in constitutive and adaptive heavy metal tolerances in hyperaccumulator and non-hyperaccumulator metallophytes. J. Exp. Bot. 53, 2381–2392.

Scheidegger, A.M., Lamble, G.M., Sparks, D.L., 1997. The kinetics of nickel sorption on pyrophyllite as monitored by x-ray absorption fine structure (XAFS) spectroscopy. J. Phys. IV 7, 773–775.

Shen, Z.G., Zhao, F.J., McGrath, S.P., 1997. Uptake and transport of zinc in the hyperaccumulator *Thlaspi caerulescens* and the non-hyperaccumulator *Thlaspi ochroleucum*. Plant Cell Environ. 20, 898–906.

Siebielec, G., Chaney, R.L., 2006. Manganese fertilizer requirement to prevent manganese deficiency when liming to remediate Ni-phytotoxic soils. Commun. Soil Sci. Plant 37, 163–179.

Siebielec, G., Chaney, R.L., Kukier, U., 2007. Liming to remediate Ni contaminated soils with diverse properties and a wide range of Ni concentration. Plant Soil 299, 117–130.

Stewart, J.M., Lingafelter, E.C., Breazeale, J.D., 1961. The crystal structure of Disaguabis (salicylaldehydato) nickel. Acta Cryst. 14, 888.

Strathmann, T.J., Myneni, S.C.B., 2004. Speciation of aqueous Ni(II)–carboxylate and Ni(II)–fulvic acid solutions: combined ATR-FTIR and XAFS analysis. Geochim. Cosmochim. Acta 68, 3441–3458.

Sun, R.L., Zhou, Q.X., Wang, X., 2006. Relationship between cadmium accumulation and organic acids in leaves of *Solanum nigrum L.* as a cadmium hyperaccumulator. Huan Jing Ke Xue 27 (4), 765–769.

Surewicz, W.K., Mantsch, H.H., Capman, D., 1993. Determination of protein secondary structure by Fourier transform infrared spectroscopy: a critical assessment. Biochemistry 32, 389–394.

Tappero, R., Peltier, E., Grafe, M., Heidel, K., Ginder-Vogel, M., Livi, K.J.T., Rivers, M.L., Marcus, M.A., Chaney, R.L., Sparks, D.L., 2007. Hyperaccumulator *Alyssum murale* relies on a different metal storage mechanism for cobalt than for nickel. New Phytol. 175, 641–654.

Tolra, R.P., Poschenrieder, C., Barcelo, J., 1996. Zinc hyperaccumulation in *Thlaspi caerulescens* 2: influence on organic acids. J. Plant Nutr. 19, 1541–1550.

Wasserman, S.R., Allen, P.G., Shuh, D.K., Bucher, J.J., Edelstein, N.M., 1999. EXAFS and principal component analysis: a new shell game. J. Synchrotron Radiat. 6, 284–286.

White, P.J., Broadley, M.R., 2009. Biofortification of crops with seven mineral elements often lacking in human diets – iron, zinc, copper, calcium, magnesium, selenium and iodine. New Phytol. 182, 49–84.

Zabinsky, S.I., Rehr, J.J., Ankudinov, A., Albers, R.C., Eller, M.J., 1995. Multiple-scattering calculations of x-ray-absorption spectra. Phys. Rev. B 52, 2995–3009.

Zhang, W.H., Cai, Y., 2003. Purification and characterization of thiols in an arsenic hyperaccumulator under arsenic exposure. Anal. Chem. 75, 7030–7035.

Zhang, L., Angle, J.S., Chaney, R.L., 2007. Do high-nickel leaves shed by the nickel hyperaccumulator *Alyssum murale* inhibit seed germination of competing plants? New Phytol. 173, 509–516.

Please cite this article in press as: McNear, D.H., et al. The hyperaccumulator *Alyssum murale* uses complexation with nitrogen and oxygen donor ligands for Ni transport and storage. Phytochemistry (2009), doi:10.1016/j.phytochem.2009.10.023